Applied Catalysis B: Environmental 239 (2018) 268–279

Contents lists available at ScienceDirect

Applied Catalysis B: Environmental

journal homepage: www.elsevier.com/locate/apcatb

A dual-function photocatalytic system for simultaneous separating hydrogen from water splitting and photocatalytic degradation of phenol in a twin-reactor

Duanxing Li[a], Joseph Che-Chin Yu[a], Van-Huy Nguyen[b,c,**], Jeffrey C.S. Wu[a,*], Xuxu Wang[d]

[a] Department of Chemical Engineering, National Taiwan University, Taipei 10617, Taiwan
[b] Department for Management of Science and Technology Development, Ton Duc Thang University, Ho Chi Minh City, Viet Nam
[c] Faculty of Applied Sciences, Ton Duc Thang University, Ho Chi Minh City, Viet Nam
[d] State Key Laboratory of Photocatalysis on Energy and Environment, Research Institute of Photocatalysis, College of Chemistry, Fuzhou University, Fuzhou 350108, China

ARTICLE INFO

Keywords:
Photocatalyst
Water splitting
Twin-reactor
Hydrogen
Phenol degradation

ABSTRACT

Coupling photocatalytic H_2 evolution and phenol degradation have drawn much attention on H_2 as clean energy and phenol as an organic pollutant to the environment. Such dual-function reaction can utilize the chemical potential of phenol oxidation to make up the chemical potential required for hydrogen evolution from water splitting. The production of H_2 thus was enhanced via the phenol oxidation. However, H_2 is still needed to be purified from the reaction products by traditional methods. In this study, we demonstrated the simultaneous separation of H_2 using a photo twin-reactor under artificial sunlight, in which the photocatalytic efficiency was substantially increased due to the inhibition of backward reaction by separating H_2 from the products directly. Three Rh-doped $SrTiO_3$ (STO) photocatalysts calcined at 900, 1100, 1200 °C (named as STO:Rh900, STO:Rh1100, and STO:Rh1200, respectively) were prepared by solid-state fusion reaction, then photo-deposition method was applied to synthesize Pt loading STO:Rh. All photocatalysts were fully characterized by XRD, XPS, UV–vis, SEM, TEM, and DLS. A single reactor and a twin-reactor (Z-scheme system) were systematically designed by using Pt/STO:Rh for H_2 evolution photocatalyst and WO_3 for phenol oxidation photocatalyst, where Fe^{3+}/Fe^{2+} pairs were served as electron transfer mediators to conduct the dual-function reaction. In the single reactor, the stoichiometric of the dual-function reaction was proposed and with high consistency to the experimental data. By using the twin-reactor, H_2 production rate increased 2.7 times, reaching 1.90 μmol g^{-1} h^{-1}, compared to that in the single reactor. Moreover, the H_2 concentration of the gas-phase products increased from 70% (in the single reactor) to 94% owing to the separation function of the twin-reactor, which would significantly reduce the cost for further purification. The effect of phenol concentration on H_2 production in the twin-reactor was also thoroughly investigated. The results showed that increased phenol initial concentration would enhance the production of H_2. With 200 μmol L^{-1} phenol, the H_2 yield (11.37 μmol g^{-1} in 6-h reaction) was increased by 20% compared to that of pure water splitting.

1. Introduction

Various inorganic and organic systems have been developed as photocatalysts for water splitting and environmental remediation driven by UV/visible light for past five decades. The photocatalytic water splitting and hydrogen generation (Eq. (1)) have been largely investigated since the "Honda–Fujishima effect" was first reported in 1972 [1–4]. However, the water-splitting reaction is thermodynamically unfavorable, and much energy input is needed to drive the reaction because of their positive molar Gibbs energy change (ΔG_m°) and molar enthalpy change (ΔH_m°) at standard conditions. Compared to the traditional hydrogen production methods such as steam reforming, photocatalytic water splitting is activated by solar energy, which is a kind of renewable and environmental friendly power supply. Also, it can be carried out under mild conditions rather than high pressure or high temperature. Although extensive studies with research interests varied from materials modification, reactor designs to mechanism investigation have been carried out [5–10], the photocatalytic water

* Corresponding author at: Department of Chemical Engineering, National Taiwan University
** Corresponding author at: Ton Duc Thang University, Ho Chi Minh City, Viet Nam.
E-mail addresses: nguyenvanhuy@tdtu.edu.vn (V.-H. Nguyen), cswu@ntu.edu.tw (J.C.S. Wu).

https://doi.org/10.1016/j.apcatb.2018.08.010
Received 15 April 2018; Received in revised form 26 July 2018; Accepted 3 August 2018
Available online 06 August 2018
0926-3373/

splitting has not been practically used yet because of the relatively low photo-efficiency.

$$H_2O \xrightarrow{h\nu \geq E_{bg},\ photocatalyst} H_2 + \frac{1}{2}O_2$$
$$\Delta H^\circ = 285.8\ KJ\ mol^{-1},\ \Delta G^\circ = 237.1\ KJ\ mol^{-1} \quad (1)$$

From the 1990s, the photocatalytic applications in environmental remediation began to draw much attention from researchers. As one of the advanced oxidization processes, photocatalytic oxidation (PCO) technology utilizes semiconductors as photocatalysts. During the PCO process, photocatalysts could produce highly reactive radical species under solar irradiation, which will further mineralize pollutants to benign substances (Eq. (2) with phenol as the model organic pollutant) [11–13]. From the thermodynamic perspective, this reaction would happen spontaneously under standard conditions and generate much energy, which is transformed from the internal chemical energy of phenol.

$$\frac{1}{14}C_6H_6O + \frac{1}{2}O_2 \xrightarrow{h\nu \geq E_{bg},\ photocatalyst} \frac{3}{7}CO_2 + \frac{3}{14}H_2O$$
$$\Delta H^\circ = -218.2\ KJ\ mol^{-1},\ \Delta G^\circ = -216.2\ KJ\ mol^{-1} \quad (2)$$

If we could construct a system to couple these two processes together, then the goal of dual-function reaction will be achieved (Eq. (3)), in which hydrogen gas will be generated (function 1), and organic pollutants could be degraded (function 2) simultaneously. From the perspective of thermodynamics, with one mole of hydrogen gas generated, the Gibbs energy change of reaction (ΔG°) decreases from 237.1 KJ of pure water splitting (Eq. (1)) to 20.9 KJ of dual-function reaction (Eq. (3)), suggesting that the dual-function reaction is more equilibrium favourable. Therefore, the H_2 production efficiency would be enhanced. Also, the change of enthalpy reaction (ΔH°) decreases from 285.5 KJ to 67.6 KJ with 1 mol of H_2 produced, meaning that the energy input is mostly reduced, which is due to the utilization of the internal chemical energy of phenol. That is, the dual-function reaction could utilize the chemical energy of phenol, which otherwise would be wasted as heat in the PCO process, to make up for the energy needed for hydrogen evolution.

$$\frac{1}{14}C_6H_6O + \frac{11}{14}H_2O \xrightarrow{h\nu \geq E_{bg},\ catalyst} \frac{3}{7}CO_2 + H_2$$
$$\Delta H^\circ = 67.6\ KJ\ mol^{-1},\ \Delta G^\circ = 20.9\ KJ\ mol^{-1} \quad (3)$$

In the PCO process in which photocatalytic technology is utilized to remove phenol, oxygen or air is usually used as the oxidizing reagent. However, to produce hydrogen gas when degrading the organic pollutants, hydrogen atoms or water should be the electron acceptor rather than oxygen. Thus, oxygen must be removed from the system; otherwise, oxygen gas would accept the photo-induced electrons and no hydrogen gas would be generated.

When conducting a photocatalytic water splitting reaction, the positions of the valence band (VB) and conduction band (CB) of photocatalysts are very critical. Compared to the redox potential of water, the evolution of H_2 may take place only when the potential of CB is more negative than $E(H^+/H_2)$, which is 0 V at pH 0. Moreover, if the potential of VB is more positive than $E(O_2/H_2O)$, which is 1.23 V at pH 0, the evolution of O_2 would occur. Therefore, photocatalysts with both CB and VB applicable for H_2 and O_2 evolution respectively can split the water directly, such as TiO_2 (E_{bg} = 3.2 eV) and ZnO (E_{bg} = 3.2 eV). However, such photocatalysts with large bandgaps can only response to UV light, which accounts for less than 5% of the whole solar spectrum. To take full advantage of the solar spectrum, photocatalysts with smaller bandgaps are developed shifting the active region of photocatalysts to visible-light range. However, many such photocatalysts can only reduce or oxidize water to produce H_2 or O_2, but they cannot perform the whole water splitting. For example, WO_3 (E_{bg} = 2.6 eV) is an excellent good water oxidizing photocatalyst with relatively poor reducing ability, while Pt/$SrTiO_3$:Rh can only conduct the H_2 evolution reaction but not the O_2 generation.

The Z-scheme mechanism is widely adopted in conducting the whole water splitting reaction under visible light irradiation. Over many years Kazuhiko Maeda has made significant contributions to review the historical development of photocatalytic water splitting systems driven by the Z-scheme principle [14]. In a Z-scheme system, O_2-generating photocatalyst and H_2-generating photocatalyst work respectively to produce O_2 and H_2, and ion pairs (i.e. Fe^{3+}/Fe^{2+}, $IO^{3-}/I-$) are used as electron transfer mediators to achieve the charge balance [5,15–17]. A novel twin-reactor was proposed to split the water by Z-scheme mechanism. In particular, H_2 evolution and O_2 evolution take place in different compartments of the twin-reactor divided by a Nafion membrane, and therefore, these two kinds of products separate with each other simultaneously when they are produced, avoiding the reverse reaction and further separation of products [5,15,18].

For the research works to now, the dual-function photo-reactions have been achieved by using different model contaminants varied from organic to inorganic pollutants, including aromatic compounds [19–21], organic dyes [22], and toxic As(III) [23]. However, all these studies were conducted in a single photocatalyst batch reaction system [19–23]. Typically, a single photocatalyst is suspended in an aqueous solution containing contaminants. When the system is irradiated by UV/Visible light, the photo-excited holes or other oxidizing species (ex. hydroxyl radicals) will degrade the pollutants, and the photo-excited electrons would reduce the water or hydrogen atoms to generate hydrogen gas. If the model pollutant is organic, then products H_2, CO, and CO_2 are mixed in the top region of the reactor, which needs further purification. If we could utilize the novel twin-reactor to conduct the dual-function reaction mimicking Z-scheme mechanism, then, pollutants degradation and H_2 generation would happen in different apartments divided by a Nafion membrane. In this way, the H_2 could be separated from other gaseous products directly as it is produced and decrease the cost for further purification of hydrogen gas.

In this study, a novel photocatalytic dual-function system was constructed to mimic the Z-scheme mechanism. The half-reaction of phenol degradation with WO_3 and the half-reaction of hydrogen evolution with Pt/$SrTiO_3$:Rh were investigated independently. Afterward, the dual-function reaction was performed in the twin-reactor with Fe^{3+}/Fe^{2+} as the electron transfer mediators. By the utilization of the twin-reactor, H_2 and phenol degradation gaseous products (CO_2 and CO) were separated instantly when they were produced that would mainly decrease the cost for further purification.

2. Experimental

2.1. Preparation of photocatalyst

There were five $SrTiO_3$ related photocatalysts tested in this research for hydrogen evolution, which was STO, STO:Rh-1000, STO:Rh-1200, STO:Rh-1300 and Pt/STO:Rh (these labels would be explained as following). The unmodified $SrTiO_3$ and $SrTiO_3$:Rh ($SrTiO_3$ doped with Rh) were prepared by the solid-state fusion method reported in the previous literature [24]. For the synthesis of $SrTiO_3$:Rh photocatalysts, typically, $SrCO_3$ (Strontium Carbonate, Showa Chemicals, 99.0%, pre-treated in air at 300 °C for 1 h), TiO_2 (Titanium Dioxide, anatase ~5 μm, Wako Pure Chemical, 99.9%) and Rh_2O_3 (Rhodium(III) Oxide, Sigma Aldrich, 99.9%) were mixed with a molar ratio of 1.00:0.99:0.01, then a few drops of CH_3OH (Methanol, Sigma Aldrich, > 99.8%) were added to help uniform mixing. After that, the mixture was heated in air at 1000 °C, 1200 °C and 1300 °C, respectively, for 10 h. The obtained $SrTiO_3$:Rh photocatalysts were denoted as STO:Rh-1000, STO:Rh-1200 and STO:Rh-1300 in which the number stands for the temperature. For the synthesis of unmodified $SrTiO_3$ photocatalysts, the procedure was similar without Rh_2O_3 precursors. $SrCO_3$ (pre-treated in the air at 300 °C for 1 h) and TiO_2 were mixed with a molar ratio of 1:1, followed by the calcination at 1000 °C for 10 h. The obtained $SrTiO_3$

photocatalysts were named as STO hereafter.

Pt nanoparticles were loaded on STO:Rh-1200 by the photo-deposition method [25]. The obtained STO:Rh-1200 photocatalyst was dispersed in 10% CH_3OH solution, and the corresponding amount of $H_2PtCl_6.6H_2O$ (Hydrogen Hexachloroplatinate(IV) Hydrate, Alfa Aesar, 99.9%) solution was added into the suspension based on the calculation that Pt accounted for 0.8 wt.% of the total synthesized photocatalysts. The resulted solution was vigorously stirred and irradiated by UV light (200 W High-Pressure Mercury Lamp, OmniCure S1500) for 90 min. After deposition, the solid samples were collected and washed with D.I. water for 3 times and dried at 80 °C overnight. After grinding, the photocatalyst was obtained and named as Pt/STO:Rh. Commercial WO_3 (Tungsten(VI) Oxide, Sigma Aldrich, 99.995%) was used directly as received.

2.2. Characterization of photocatalysts

The crystalline structures of the samples were confirmed by powder X-ray diffraction (XRD) on a Rigaku Ultima IV diffractometer (CuKα radiation, λ = 0.15418 nm) at a scanning rate of 10° (2θ) min^{-1}. The UV–vis diffuse reflectance spectra (DRS) were recorded by a Varian Cary-300 spectrophotometer equipped with an integrating sphere, and the light absorption range was measured between 200 and 800 nm. To observe the morphology of photocatalysts, a field emission scanning electron microscopy (FE-SEM, Nova NanoSEM 230) equipped with an energy dispersive X-ray spectroscopy (EDS) detector and a high-resolution transmission electron microscopy (HR-TEM, Tecnai G^2 F20) were both conducted in this research. Also, the selected area electron diffraction (SAED) patterns of photocatalysts were obtained by the as-mentioned HR-TEM. Dynamic light scattering (DLS, Malvern Zetasizer) was used to analyze the average particle size and size distribution of photocatalyst particles. The specific surface area was measured by Brunauer-Emmett-Teller (BET) tests using ASAP 2010 (Micromeritics Instruments) analyzer. Before the measurement, the samples were dried in an oven at 120 °C for 24 h to remove water. The surface elements chemical status of photocatalysts was investigated by an X-ray photoelectron spectroscopy (XPS, Thermal Fisher Scientific Theta Probe) equipped with an Al-Kα X-ray source (1486.6 eV), and the pass energy of detector was 200 eV. In XPS analysis, all the samples were prepared by the same procedure, where the photocatalyst powders were tableted first and cleaned by Ar ion cluster before the measurement. C(1 s) = 284.3 eV was utilized as the standard for energy correction for all patterns.

2.3. Apparatus and procedures

In this study, two kinds of reactor systems were adopted to conduct the experiments, which were the single batch reactor and the twin-reactor. Firstly, half-reactions of phenol oxidation reaction and hydrogen evolution reaction were conducted, independently, in the single batch reactor to optimize the reaction conditions. After that, the dual-function reaction of simultaneous hydrogen production and phenol degradation was carried out in a single batch reactor and then a twin-reactor. The light source was provided by a 300 W Xenon lamp (Newport, Model 66902) equipped with an AM1.5 G filter to simulate the sunlight that has the same power and spectral distribution of the sun at 48.5° zenith angle [26]. A series of blank experiments were performed to evaluate the effect of photolysis, adsorption by photocatalyst and homogeneous reaction between phenol and Fe^{3+}.

For the half-reaction of hydrogen evolution, 120 mL of deionized water (D.I. water) was poured into the reactor, and then 0.1 g of different kinds of hydrogen evolution photocatalysts were suspended in the solution. Afterward, 2 mmol L^{-1} of $FeCl_2$ (Sigma Aldrich, 99.0%) was added to act as the hole acceptor, and the pH value of the solution was adjusted to 2.4 by sulfuric acid (Sigma Aldrich, 96%) to avoid the precipitation of Fe^{2+}. Before the light irradiation, the system was purged by Ar (99.99%) for 1 h. After the Xe lamp was turned on, 0.5 mL of gas-phase products were sampled every 2 h and detected by a GC-TCD (GC-2000, China Chromatography Co.) equipped with a molecular sieve 5 A column. For the half-reaction of phenol oxidation, 0.08 g of WO_3 photocatalyst was suspended in 180 mL $FeCl_3$ (Sigma Aldrich, 97.0%) solution (Fe^{3+} = 2 mmol L^{-1}). A certain amount of phenol (Sigma Aldrich, > 99.5%) stock solution was added to adjust the initial phenol concentration to be 50, 100, 150 and 200 μmol L^{-1} respectively. N_2 gas (99.99%) was purged throughout the suspension for 1 h to remove the dissolved oxygen before the Xe lamp was turned on. During the photoreactions, 0.5 mL gas-phase products were detected every 2 h by a GC-FID (GC-9800, China Chromatography Co.) equipped with a methanizer packed with Ni catalyst and a Porapak QS column. This methanizer can convert possible CO, CO_2 into CH_4 with H_2 at 633 K. 3 mL of liquid sample was collected every 2 h for further measurement of phenol by high-performance liquid chromatography (HPLC) equipped with a C18 column (5 μm, 4.6 mm I.D.*250 mm) and a PDA detector (270 nm for measurement). The mobile phase was composed of 68.6% D.I. water, 30% methanol and 1.4% acetic acid with a flow rate of 1 mL min^{-1}. The total organic carbon analyzer (TOC analyzer, Aurora Model 1030 W/1088) equipped with an NDIR detector under wet chemistry oxidation method. The following equations define both phenol removal % and TOC removal %:

$$\text{Phenol removal } (\%) = \frac{[C]_{\text{bef. irradiation}} - [C]_{\text{aft. irradiation}}}{[C]_{\text{bef. irradiation}}} \quad (4)$$

$$\text{TOC removal } (\%) = \frac{[TOC]_{\text{bef. irradiation}} - [TOC]_{\text{aft. irradiation}}}{[TOCl]_{\text{bef. irradiation}}} \quad (5)$$

For the dual-function reaction conducted in a single batch reactor, the reactor was shown in Fig. 1(a). The primary container was made in Pyrex with the volume of 310 mL and sealed by a stainless-steel cover with O-ring. There was a sampling vent with septa on the cover. Typically, 0.1 g of WO_3 and 0.25 g of Pt/STO:Rh photocatalysts were suspended in 220 mL water solution containing 1 mM $FeCl_3$ and 1 mM $FeCl_2$. The pH value of the solution was adjusted to 2.4 by sulfuric acid. The initial phenol concentration was 200 μmol L^{-1}. For every 2 h, 0.5 mL gas-phase products were analyzed to acquire the amounts of photo-generated hydrogen, and carbon monoxide, carbon dioxide by the GC-TCD and GC-FID, respectively. Also, 3 mL liquid sample was collected every 2 h for the analysis of phenol concentration and TOC amount same as in phenol oxidation half reaction. For the dual function reaction conducted in a twin-reactor as shown in Fig. 1(b), the pyrex reactor was divided by a circular Nafion membrane (NafionTM 117, Sigma Aldrich) into two compartments, which were named as hydrogen evolution side (right side of the figure) and phenol oxidation side (left side of the figure), respectively. The Nafion membrane was Fe-ion pre-exchanged to allow the permeation of Fe ions. In the hydrogen evolution side, 0.25 g Pt/STO:Rh was dispersed in 220 mL 2 mM $FeCl_2$ solution (pH = 2.4), and Ar (99.99 V%) was used to purge this side for 1 h before the light irradiation. In the phenol oxidation side, 0.1 g WO_3 was suspended in 220 mL 2 mM $FeCl_3$ solution (pH = 2.4) containing different amount of phenol (50, 100, 150 and 200 μmol L^{-1}), and this side was purged by N_2 (99.99%) for 1 h before the light irradiation. During the irradiation process, both gas and liquid phase products, which were collected in every 2 h, were analyzed by GC-TCD, GC-FID, HPLC and TOC analyzer.

3. Results and discussion

3.1. Characterization of photocatalyst

X-ray diffraction spectrometry was conducted to investigate the crystalline structures of the prepared photocatalysts. Fig. 2 shows the XRD patterns of WO_3 and five kinds of $SrTiO_3$ related hydrogen evolution photocatalysts. For STO, photocatalysts with Rh doping under 3

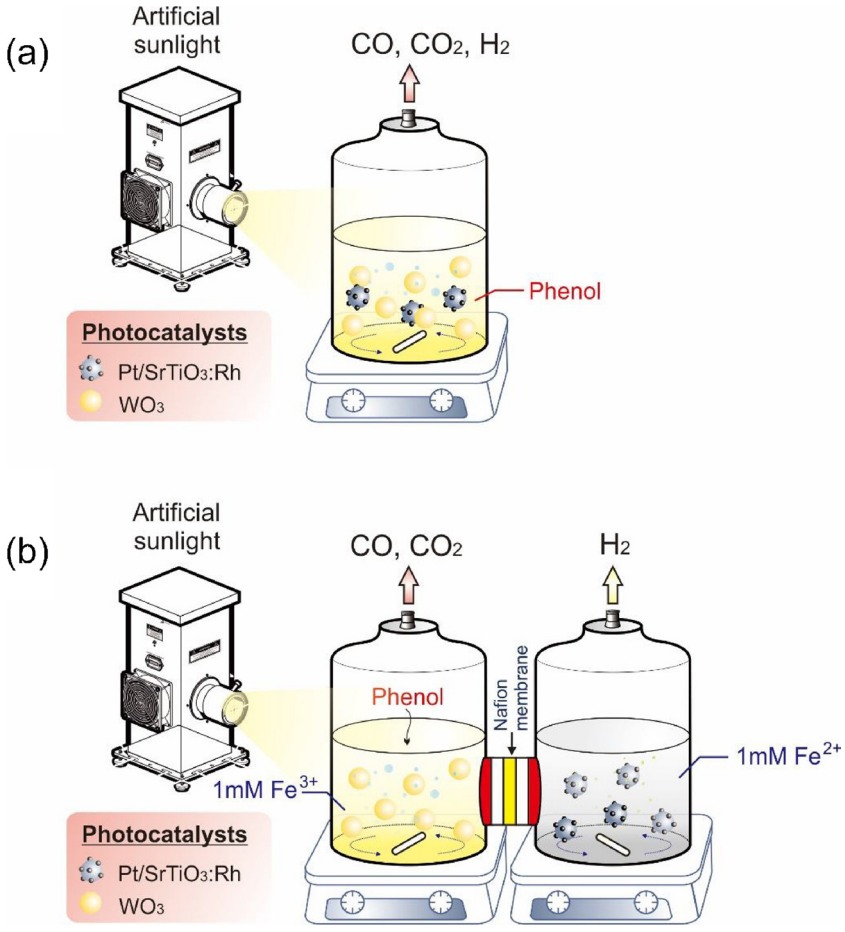

Fig. 1. Illustration of dual function reaction conducted in (a) a single batch reactor and (b) a twin-reactor.

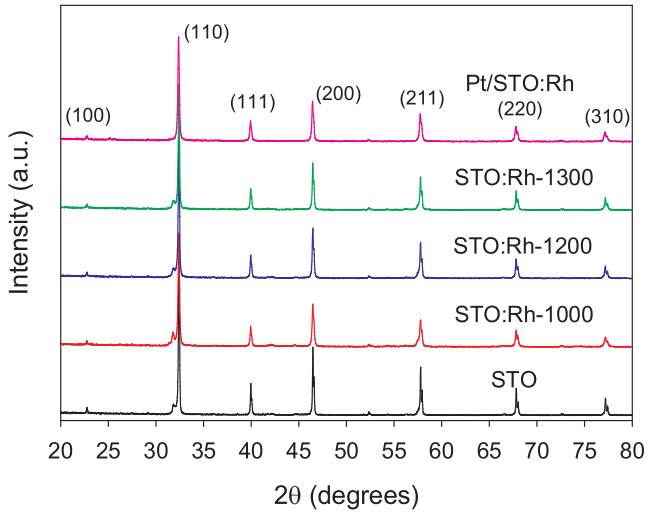

Fig. 2. XRD patterns of STO, STO:Rh-1000, STO:Rh-1200, STO:Rh-1300 and Pt/STO:Rh photocatalysts.

different calcination temperatures STO:Rh-1000, STO:Rh-1200 and STO:Rh-1300, and photocatalysts with both Rh doping and Pt loading Pt/STO:Rh, characteristic peaks at $2\theta = 22.8^{\circ}$, 32.4°, 40.0°, 46.5°, 52.3°, 57.8°, 67.8°, 72.6° and 77.2° were observed in all the patterns, which were in good agreement with the perovskite structure (JCPDS, No. 74-1296), indicating that the photocatalysts were successfully prepared. After the doping of Rh, the positions of characteristic peaks in STO:Rh-1000, STO:Rh-1200 and STO:Rh-1300 remained the same as STO. There were no observed peak shifts which were induced by the doping of Rh among STO:Rh-1000, STO:Rh-1200 and STO:Rh-1300. This result might be because the doping amount of Rh was too low (< 1% molar) to change the d-space of crystalline structures. For the Pt/STO:Rh photocatalyst, the photo-deposition method employing high-intensity UV light did not destroy the crystal structure of STO:Rh. However, the diffraction peaks of Pt were absent from Pt/STO:Rh, which might be caused by the low concentration of Pt in the photocatalyst. The diffraction peaks of the commercial WO_3 photocatalyst were all consistent with the typical orthorhombic WO_3 (JCPDS, No. 83-0951).

Fig. 3 shows the UV–vis absorption spectra of the five hydrogen-generating photocatalysts and the phenol-oxidizing WO_3 photocatalyst. The STO photocatalyst had the central absorption edge below 390 nm, where is the range of UV light. For the STO:Rh photocatalysts prepared under three different calcination temperatures, they showed light absorption in the visible range to a different extent, meaning that the Rh doped photocatalysts STO:Rh-1000, STO:Rh-1200 and STO:Rh-1300 were all visible-light responsive. However, the absorption increases of STO:Rh-1000 was not apparent, it only exhibited little absorption around 400–500 nm. When the calcination temperature was raised to 1200 °C, and 1300 °C, the absorption in 400–500 nm was significantly enhanced and there existed a low absorption peak at about 500–650 nm. It should be noted that although STO:Rh-1300 calcination temperature was higher than that of STO:Rh-1200, these photocatalysts had a similar UV–vis absorption property. Pt/STO:Rh was prepared by loading Pt particles on the surface of STO:Rh-1200 by the photo-deposition method. These two photocatalysts showed almost the same UV–vis spectra, suggesting that the influence of Pt particles on the light absorption properties of the photocatalyst was negligible in our

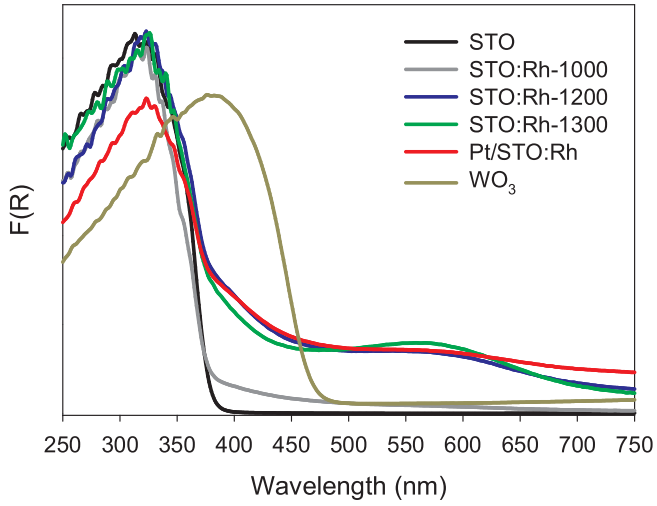

Fig. 3. UV–vis spectra of STO, STO:Rh-1000, STO:Rh-1200, STO:Rh-1300, Pt/STO:Rh, and WO_3 photocatalysts.

experimental conditions (the amount of Pt was 0.8 wt.%). The absorption edge of commercial WO_3 was around 400–480 nm in a visible light region corresponding to its green color.

The reason why Rh doping would change the light absorption characteristics of photocatalysts is that the doped Rh^{3+} would provide an extra electron donor level which is more positive. Electrons need less energy to be excited from such extra donor level to the conduction band level, making the Rh doped photocatalysts visible light responsive. Moreover, the energy band gap of STO:Rh would be slightly decreased due to the hybridization of extra donor level with O(2p) orbital energy level [24]. The energy bandgaps of the photocatalysts can be estimated from the onset of the absorption edge from UV–vis spectra, the BET surface area and the derived values of prepared photocatalysts were summarized in Table 1.

Fig. 4 showed the morphology of photocatalysts, which was characterized by SEM. It is apparent that the $SrTiO_3$ related photocatalysts in (a)–(e) had a cubic shape and a smooth surface. The particle sizes of them were all around 200–300 nm with the BET surface area of 3.79–4.01 $m^2 g^{-1}$. Also, all photocatalysts except WO_3 showed fusion phenomena and had an invisible boundary, whereas the boundary of WO_3 photocatalyst was clear. The surface compositions of all photocatalysts used in hydrogen evolution reaction were analyzed by energy dispersive X-ray spectroscopy when conducting SEM. The Sr:Ti:O values were summarized in Table 1. All the detected surface compositions were close to the theoretical value, which is 1.00:0.99:3.00 (Sr:Ti:O). Moreover, there were no Pt or Rh signals detected due to their relatively low contents.

TEM was also conducted in this research to explore the morphology and crystalline structure of the photocatalysts. The results were shown in Fig. 5. The particles showed cubic shape with size about 200–300 nm, they fused to each other, and the interfaces cannot be identified. There were some small particles existing on the surface of the photocatalyst in (d), which was the evidence of Pt deposition. The Pt particles were well-dispersed with size in the range of 3–5 nm. The SAED patterns of the three photocatalysts all showed perovskite structure with a spot like diffraction patterns. The lattices of (110), (211), (220) and (111) were observed, which were in good agreement with XRD results.

Table 1
Properties of the photocatalysts.

Entry	Photocatalyst	Composition (Sr:Ti:O)	Bandgap (eV)	Particle Size (nm)	BET surface area ($m^2 g^{-1}$)
1	WO_3	N/A	2.6	N/A	4.10
2	STO	1.0 : 1.0 : 2.7	3.3	238	3.80
3	STO:Rh-1000	1.0 : 0.9 : 3.7	3.2	244	3.79
4	STO:Rh-1200	1.0 : 0.9 : 4.2	3.0	252	3.80
5	STO:Rh-1300	1.0 : 1.0 : 2.8	3.0	280	3.83
6	Pt/STO:Rh	1.0 : 1.0 : 3.6	3.0	196	4.01

Dynamic light scattering method was utilized to obtain the average particle sizes and size distribution of photocatalysts. The results were shown in Table 3. For the STO photocatalyst, the DLS result showed a narrow size distribution concentrating from 190 nm to 295 nm, and the average particle size was 238 nm. The average particle sizes of all the photocatalysts were listed in Table 1. For STO:Rh photocatalysts calcined under three different temperatures, the average particle size increased from 243.8 nm to 279.8 nm along with calcination temperature from 1000 to 1300 °C, indicating the higher calcination temperature made the particles fused and aggregated easily under the solid-state reaction method.

The surface composition of the photocatalysts was analyzed by XPS as shown in Fig. 6. Fig. S2 shows the wide scan of Pt/STO:Rh with the characteristic peaks of O(1 s), Ti(2p), Rh(3d), Sr(3d) and Pt(4f) at 531 eV, 454 eV, 307 eV, 134 eV and 71 eV, respectively. Fig. 6(a) is the detailed analysis of Pt(4f) core level region of Pt/STO:Rh. The spectrum, formed by the two spin-orbit components $4f_{7/2}$ and $4f_{5/2}$, is characterized by two doublets corresponding to two different chemical states of Pt. The position of the $4f_{7/2}$ lines, at 71.2 eV and 73.4 eV are typical of a metallic state (Pt°) and of a highly oxidized state (Pt^{2+}), respectively. Fig. 6(b–d) shows the XPS of Rh(3d) core level region of three STO:Rh photocatalysts which are prepared under different calcination temperatures. Characteristic peaks at 307.8 eV and 313.0 eV were observed which corresponded to $3d_{5/2}$ and $3d_{3/2}$ of Rh^{3+} state, while the peaks at 309.3 eV and 314.0 eV corresponded to $3d_{5/2}$ and $3d_{3/2}$ of Rh^{4+} state. The doping of Rh into the lattice of STO structure would lead to the formation of Rh^{4+}, exhibiting the mixture of oxidative states (Rh^{3+} and Rh^{4+}). It is believed that the doping of Rh would afford extra electron donor level which is more positive, making the semiconductor photocatalysts more visible-light responsive. In this research, for STO:Rh-1200 and STO:Rh-1300 photocatalysts, the Rh peak intensities were stronger, indicating that there are more Rh in the surface of the photocatalysts STO:Rh-1200 and STO:Rh-1300. That is the reason why these two photocatalysts had enhanced absorption in visible range than STO:Rh-1000 in UV–vis spectra.

3.2. Half-reactions of hydrogen evolution and phenol degradation

Hydrogen evolution half-reaction utilizing different photocatalysts were conducted to estimate which photocatalyst has the best efficiency before the dual function reaction of simultaneous hydrogen evolution and phenol degradation. Typically, 0.1 g of different kinds of photocatalysts were dispersed in 120 mL $FeCl_2$ solution (2 mM, pH = 2.4). During the reaction, Fe^{2+} acted as the electron donor (Eq. (6)), and the amount of produced hydrogen was detected by GC-TCD every 2 h.

$$2\,Fe^{2+} + 2\,H_3O^{+} \rightarrow H_2 + 2\,Fe^{3+} + 2\,H_2O \quad (6)$$

The hydrogen evolution results were shown in Fig. 7. In the experiments, there was no hydrogen detected when using STO photocatalyst. That is, STO was without any hydrogen evolution capability under the experimental conditions. The main reason is that the energy bandgap of STO was 3.3 eV and the light source in the experiment was mainly in the visible range, which cannot excite STO to produce electron-hole pairs that can participate in the hydrogen evolution half-reaction. For the STO:Rh-1000, STO:Rh-1200 and STO:Rh-1300 photocatalysts, they all showed hydrogen production capabilities to different extent under the experiment conditions, and the average hydrogen evolution rates were 0.08 μmol $g^{-1} h^{-1}$, 1.74 μmol $g^{-1} h^{-1}$ and 1.00 μmol $g^{-1} h^{-1}$, respectively. When Rh was doped into STO photocatalysts at different calcination temperatures to form STO:Rh-1000,

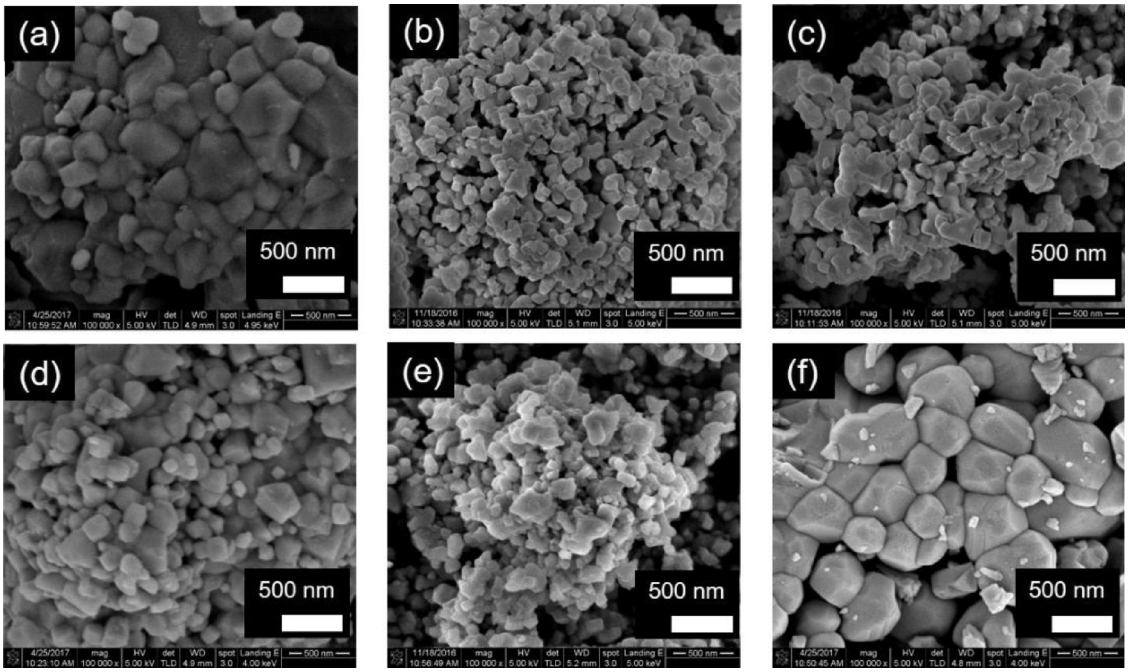

Fig. 4. SEM images of (a) STO, (b) STO:Rh-1000, (c) STO:Rh-1200, (d) STO:Rh-1300, (e) Pt/STO:Rh, and (f) WO_3 photocatalysts.

STO:Rh-1200 and STO:Rh-1300 photocatalysts, extra electron donor levels were introduced inside the bandgap. As a result, the photocatalysts could be excited by the visible light and reduce the water or hydrogen atoms to produce hydrogen gas. The hydrogen evolution amount of STO:Rh-1000 was relatively low since it had weak absorption in visible light range compared to STO:Rh-1200 and STO:Rh-1300. The STO:Rh-1200 and STO:Rh-1300 had similar light absorption characteristics, while STO:Rh-1200 showed better hydrogen production efficiency. It is because the particle size of photocatalysts increased with the higher calcination temperature (Table 1). Therefore, the photo-excited electrons and holes diffuse through the more extended pathway to the surface of the photocatalysts STO:Rh-1300, which increased the possibilities of electron-hole recombination and decreased the photocatalytic efficiency [27,28].

To further increase the photocatalytic hydrogen production efficiency of STO:Rh-1200 photocatalyst, Pt was loaded on the surface of STO:Rh-1200 as a co-catalyst in this research by the photo-deposition method, and the profiles of hydrogen evolution results were also shown in Fig. 7. As expected, the production of hydrogen will gradually reduce as the organic compound is depleted. Apparently, the hydrogen evolution efficiency of Pt/STO:Rh was primarily enhanced by the Pt loading on STO:Rh-1200. The hydrogen evolution rate was 3.97 μmol g^{-1} h^{-1} for Pt/STO:Rh. Many studies have proved that the noble metal (Pt) on the surface of photocatalysts would act as an electron trap and avoid the recombination of electron-hole pairs [27,29,30]; on the other hand, the noble metal would chemically adsorb hydrogen atoms and increase the active site amounts on the surface of the photocatalysts. In this study, Pt/STO:Rh was chosen as the optimum hydrogen evolution

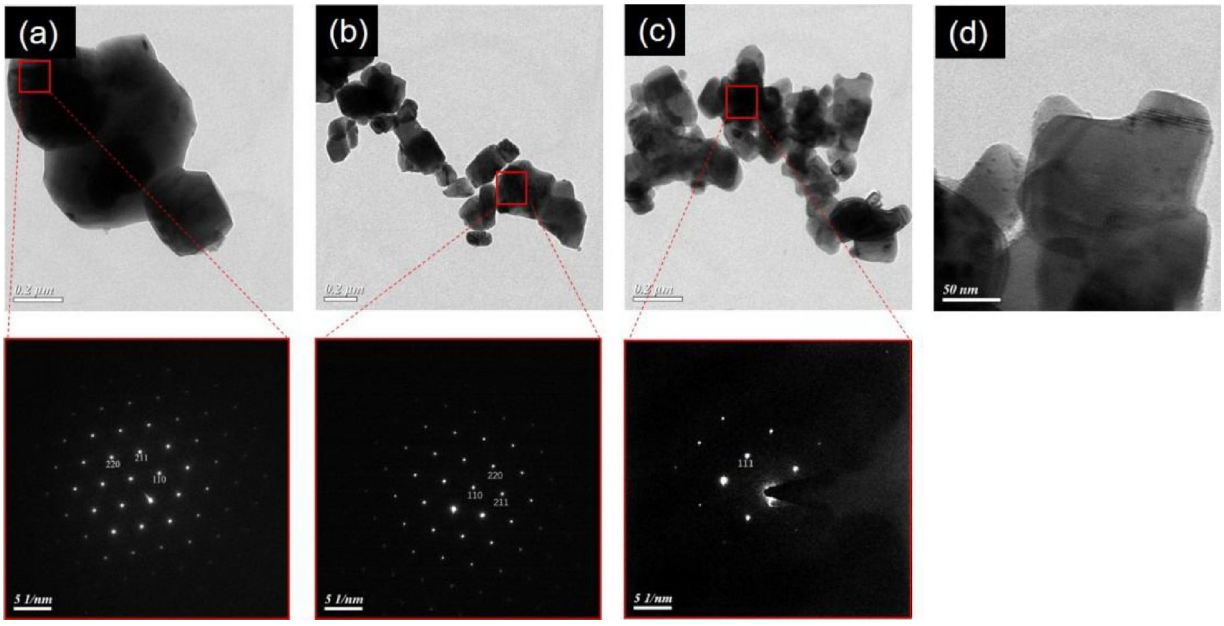

Fig. 5. TEM images and SAED patterns of (a) STO, (b) STO:Rh-1200, and (c–d) Pt/STO:Rh photocatalysts.

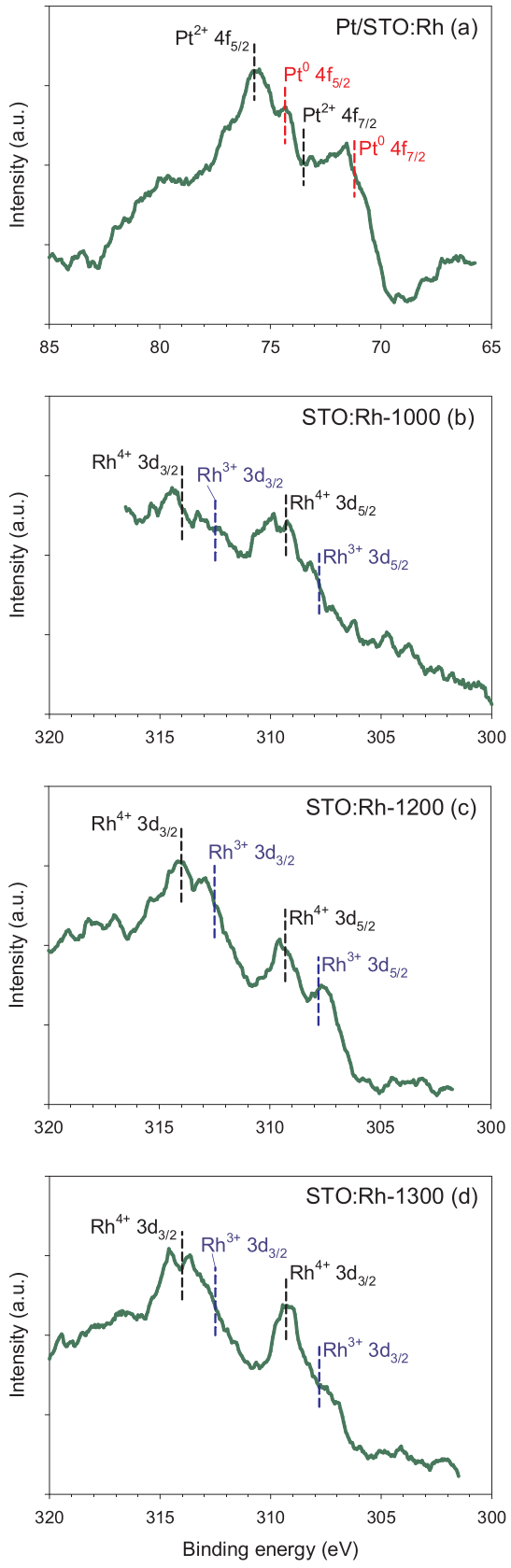

Fig. 6. XPS of Pt(4f) core level region of (a) Pt/STO:Rh, and XPS of Rh(3d) core level region of (b) STO:Rh-1000, (c) STO:Rh-1200, (d) STO:Rh-1300 photocatalysts.

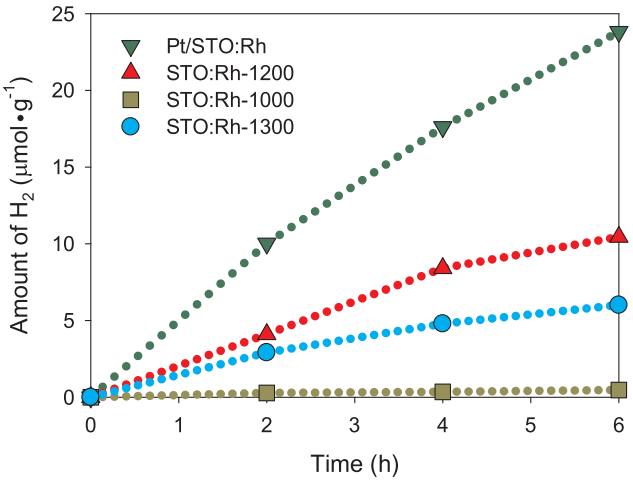

Fig. 7. A screening of hydrogen evolution in half-reaction over different photocatalysts (Experimental conditions: 120 mL water contanining 2 mM $FeCl_2$; pH = 2.4; the amount of photocatalyst: 0.1 g; 300 W Xe Lamp equipped with an AM1.5 G filter; single reactor).

photocatalyst and would be utilized in the further dual function reaction.

In our research, phenol oxidation half-reaction was also conducted before the dual function reaction. Typically, 0.0818 g WO_3 was dispersed in 180 mL $FeCl_3$ solution (2 mM, pH = 2.4), and different concentrations of phenol (50 μmol L^{-1}, 100 μmol L^{-1}, 150 μmol L^{-1} and 200 μmol L^{-1}) were added into the system to investigate the effect of initial phenol concentration. Fig. 8(a) illustrates the relationship between the phenol concentration and irradiation time. The phenol was degraded to a different extent in systems with different phenol initial concentration. During the reaction, no hydrogen gas was detected, indicating that Fe^{3+} was the electron acceptor which was reduced to Fe^{2+}, as shown in Eq. (7). In the system, the photo-excited holes may oxidize the phenol directly. Also, some oxidizing species would be generated according to Eqs. (8)–(11). The photo-excited holes may react with water to produce hydroxyl radicals (OH·) as Eq. (8), and photo-excited electrons may reduce oxygen to produce superoxide radicals (O_2^-•) as Eq. (9) and hydroperoxy radicals (HO_2·) as Eq. (10), which might further react to produce hydroperoxide (H_2O_2) as Eq. (11). Since the systems had been purged by N_2 for an hour before the reaction, the oxygen may be induced into the systems by photocatalytic water oxidation during the irradiation. Jaeger utilized the spin trapping and electron spin resonance technologies to evidence for the existence of (OH·), (O_2^-•), and (HO_2·) in their water splitting research by using TiO_2 photocatalyst [31]. Moreover, Stylidi indicated that (HO_2·) would further produce hydroperoxide in their research of acid orange 7 degradations by TiO_2 [32].

$$\text{Phenol} + Fe^{3+} \xrightarrow{\text{Step I}} \text{Intermediates} \xrightarrow{\text{Step II}} CO_2 + H_2O + Fe^{2+} \quad (7)$$

$$H_2O + h^+ \rightarrow OH\bullet + H^+ \quad (8)$$

$$O_2 + e^- \rightarrow O_2^-\bullet \quad (9)$$

$$O_2^-\bullet + H^+ \rightarrow HO_2\bullet \quad (10)$$

$$HO_2\bullet + H^+ + e^- \rightarrow H_2O_2 \quad (11)$$

It was found that phenol would react with Fe^{3+} under irradiation without photocatalyst. In this study, the blank test of homogeneous reaction between phenol and Fe^{3+} were conducted to estimate the contribution of homogeneous effect to the removal of phenol and TOC. Typically, 2 mM $FeCl_3$ and different concentrations of phenol were mixed in a single batch reactor. The phenol and TOC removal percentages were shown in Fig. 8(b) as an orange and green column,

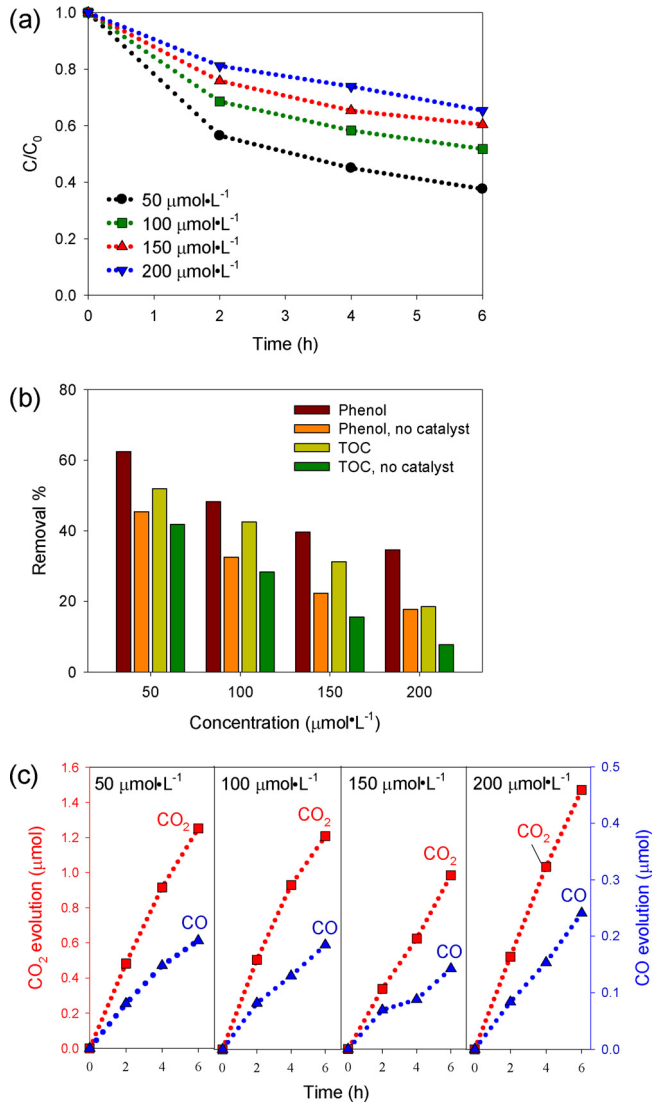

Fig. 8. A screening of phenol degradation in half-reaction over different initial concentrations of phenol: (a) the dependent behavior of the change of phenol to the reaction time, (b) the comparison of phenol and TOC removal% in the presence/ absence of WO_3 photocatalyst during the 6-h reaction, (c) the typical time course of CO_2 and CO evolution from photocatalytic environmental remediation. (Experimental conditions: 180 mL water containing 2 mM $FeCl_3$; pH = 2.4; the amount of WO_3 photocatalyst: 0.08 g; initial concentrations of phenol: 50–200 μmol L^{-1}; 300 W Xe Lamp equipped with an AM1.5 G filter; single reactor).

respectively. For the phenol degradation, homogeneous effect accounted for 50–72 % of total removal. While for the TOC removal, the homogeneous effect contributed around 42–80 %. Blank test of direct photolysis was conducted for the system with 150 μmol L^{-1} phenol (without the presence of photocatalyst or Fe^{3+} in system), it was found that 4% of phenol was removed in 6-h irradiation and no apparent CO or CO_2 was detected. Another blank test without light irradiation (150 μmol L^{-1} phenol, with photocatalyst and Fe^{3+} in system) was carried out to investigate the effect of adsorption of phenol on the photocatalyst surface. Results (not shown) showed that the C/C_0 value fluctuated around 1, indicating that negligible phenol was adsorbed on the photocatalyst surface under equilibrium state.

The effect of initial phenol concentration on phenol removal percentage was investigated, and then the removal percentage within 6-h irradiation is shown in Fig. 8(b). The removal of phenol decreased with increasing phenol initial concentration. When 50 μmol L^{-1} phenol was added, the phenol removal percentage within 6 h was 62%. Nonetheless, when the initial concentration was increased to 200 μmol L^{-1}, the phenol removal percentage dropped to 34% due to the total amount of active sites remained the same for a fixed dose of the photocatalyst. With the increase of phenol concentration, the limiting surface active sites for the reaction would restrict the rate of phenol decomposition [33,34]. The total organic carbon (TOC) amount, which is a crucial factor to indicate the degree of water contamination, was also measured during the reaction as shown in Fig. 8(b). The TOC removal was around 20–50 % in the systems with the different initial amount of phenol, suggesting that part of phenol was entirely mineralized to inorganic products. The decrease of TOC removal % with increasing phenol concentration could also be explained by the limitation of surface active sites. For a fixed concentration of phenol, the removal percentage of TOC was always lower than that of phenol, indicating that some organic intermediates existed in the system which contributed to the amount of TOC. This result is consistent with the previous report that catechol, hydroquinone, benzoquinone and organic acids are common intermediates that exist in phenol photocatalytic oxidation systems [11,13,35]. To acquire more information about the reaction pathway of phenol oxidation, Fig. 8(c) illustrates the evolution of CO_2 and CO, which were detected by converting to CH_4 using the GC-FID equipped with a methanizer. It shows that their amounts both increased during the photoreaction and CO_2 was the main gaseous products.

3.3. Dual-function photoreaction in a single reactor

The dual function reaction of phenol degradation and simultaneous hydrogen production was conducted in a single reactor before it was conducted in the twin-reactor. In this section, Pt/STO:Rh and WO_3 were used as hydrogen evolution photocatalyst and phenol degradation photocatalyst, respectively, and Fe^{3+}/Fe^{2+} pairs were added as the electron transfer mediators. After the light source was turned on, the hydrogen evolution, phenol concentration, and TOC amount were measured in every 2 h. The data was shown in Fig. 9(a). In the 8-h reaction, the hydrogen evolution was 5.59 μmol g^{-1} which corresponded to the rate of 0.70 μmol g^{-1} h^{-1}. It is noted that the degradation of phenol occurred mainly in the first 4 h, and the removal percentage was around 13%. In the range of the 4–8 h, the concentration of phenol (C/C_0) fluctuated around 0.87, suggesting that no more phenol was degraded during this period. For the dual function reaction, the photo-induced electrons would reduce hydrogen atoms to produce H_2, and organic pollutants consumed the electron holes so that no carrier accumulation exits inside the photocatalysts. However, during the 4–8 h, the amount of H_2 evolution still increased even if no phenol was oxidized during this range. It is suspected that the photo-induced holes on photocatalysts may be consumed by the oxidation of organic intermediates, such as catechol, hydroquinone, bezoquinone or hydroxyl hydroquinone, and hydrogen atoms were kept reduced by electrons in photocatalysts to produce hydrogen gas. This assumption could be evidenced by the TOC change as shown in Fig. 9(a). In the 4–8 h, the TOC in the system decreased, meaning that the organic intermediates of phenol degradation were oxidized during this period. Because the reaction system had been purged by N_2 to avoid air, and water was not a good oxygen donor or electron acceptor compared to O_2, the mineralization of phenol was limited. Similar results were obtained by Kim et al. [19,21], in which water was utilized as the oxidizing reagent to remove organic pollutants (e.g. phenol), and no significant TOC removal was measured.

The dual function reaction could be analyzed as the addition of two reactions, namely the photocatalytic water splitting and the photocatalytic phenol oxidation by oxygen evolved from water splitting [36]. However, it is important to note that many kinds of oxidative species, such as OH radical and hydroperoxide, would be produced in the photocatalytic water splitting reaction, which would further oxidize the phenol. However, whatever the oxidative species were, the ideal dual

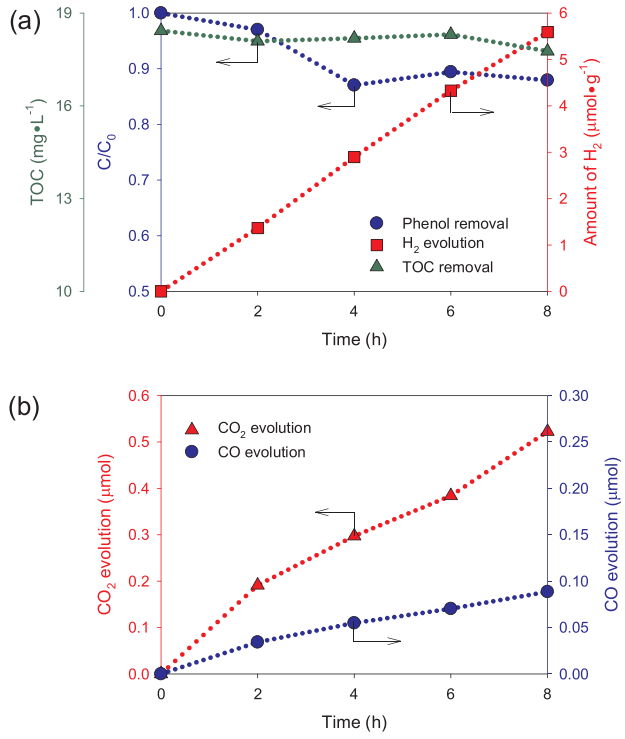

Fig. 9. Dual function reaction conducted in a single reactor with initial phenol concentration of 200 μmol L^{-1} (a) Hydrogen production, phenol degradation, and TOC change, and (b) CO_2 and CO evolution. (Experimental conditions: 220 mL water containing 1 mM $FeCl_2$ and 1 mM $FeCl_3$; pH = 2.4; photocatalysts: 0.1 g of WO_3 and 0.25 g of Pt/STO:Rh; initial concentrations of phenol: 200 μmol L^{-1}; 300 W Xe Lamp equipped with an AM1.5 G filter; single reactor).

function reaction could be represented as Eqs. (12) and (13), in which phenol was oxidized to CO or CO_2 and hydrogen was produced simultaneously. For the dual function reaction conducted in a single reactor, the time-dependent CO and CO_2 production are shown in Fig. 9(b). The main phenol oxidation gaseous product was CO_2 with a yield of 0.52 μmol during the 8-h reaction, and the amount of CO was relatively small with a yield of 0.09 μmol during the 8-h reaction.

$$\frac{1}{14}C_6H_6O + \frac{11}{14}H_2O \xrightarrow{photocatalyst} \frac{3}{7}CO_2 + H_2 \quad (12)$$

$$\frac{1}{8}C_6H_6O + \frac{5}{8}H_2O \xrightarrow{photocatalyst} \frac{3}{4}CO + H_2 \quad (13)$$

Mass balance of gaseous products H_2, CO_2 and CO were conducted according to Eqs. (12) and (13), in which 7/3 mol H_2 would be produced with 1 mol CO_2 evolved and, similarly, 4/3 mol H_2 would be produced with 1 mol CO evolved. Therefore, the theoretical H_2 yield could be estimated from CO and CO_2 amount measured in the experiments. Then, the estimated theoretical H_2 yield was compared with the real H_2 yield detected from the experiments. The mass balance calculation results were shown in Table 2. From the results, it is apparent that H_2 yields calculated based on Eqs. (12) and (13) were very similar to those measured in the experiments, indicating that it is reasonable to use Eqs. (12) and (13) to describe the dual function reactions happened in the single reactor. The simultaneous production of hydrogen and photo-degradation of organic compound through photocatalysis were successfully achieved.

3.4. Dual-function photoreaction in a twin-reactor

In the single reactor, the products H_2, CO_2, and CO were mixed in the top zone of the reactor, which needed further H_2 separation process if H_2 would be utilized as an energy source. In this research, a novel twin-reactor was adopted to conduct the dual function reaction to directly separate the H_2 from other gaseous products as it was produced. In this way, the H_2 and other gaseous products (CO_2 and CO) would be produced in different parts of the twin-reactor. Thus, H_2 would be separated directly as it is produced. As shown in Fig. 1(b), the twin-reactor was separated into two parts by a Nafion membrane. In the phenol oxidation part, 0.1 g WO_3 was dispersed in 200 μmol L^{-1} phenol solution containing 2 mM $FeCl_3$. For the hydrogen evolution part, 0.25 g Pt/STO:Rh was added to 2 mM $FeCl_2$ solution. The initial solution pH was adjusted to 2.4 to avoid the precipitation of Fe^{2+} or Fe^{3+}, and two 300 W Xe lamps were utilized as the light source. In the photoreaction, phenol would be oxidized by the photo-induced holes on WO_3 and produce CO_2 and CO in the phenol oxidation side, while H_2 would be evolved by the photo-induced electrons on Pt/STO:Rh in the other side. Fe^{3+} and Fe^{2+} would accept the electrons on WO_3 and holes on Pt/STO:Rh, respectively, and mutually diffuse through the Fe-ion exchanged Nafion membrane to achieve the charge balance of photocatalysts. The diffusion of the electron mediator, Fe^{2+}/Fe^{3+}, through the Fe-ion exchanged Nafion membrane had been investigated in a previous study [15]. The counter diffusion of Fe^{3+} and Fe^{2+} ions toward the opposite compartment is observed and reached charge balance. The result showed that the transfer rate of mediator ions was remarkably higher than the photo-reaction rate, indicating that membrane did not delay the photocatalytic reaction in the twin reactor.

The time-dependent variation profiles of phenol concentration, H_2 yield, and TOC amount were shown in Fig. 10. In the 6-h reaction, the H_2 evolution rate was stable at 1.90 μmol g^{-1} h^{-1}, which was around 2.7 folds of that in a single reactor. At the same time, 20–22 % of TOC and phenol was removed, while in the single reactor, only 4% and 13% of TOC and phenol, respectively, were removed. The reason why reaction efficiency was increased when using the twin-reactor was that the two kinds of photocatalysts were separated on different sides of the twin-reactor, which avoided the screening effect of photocatalysts and enhanced the photocatalytic efficiency.

To evaluate the efficiency of products separation in the twin-reactor, the concentrations of H_2, CO_2 and CO in both hydrogen evolution side and phenol oxidation side were measured by GC-TCD and GC-FID when conducting the dual function reaction. After 6-h irradiation, the gas phase compositions inside reactors were calculated, and the results

Table 2
Mass balance calculation of gaseous products for the dual function reaction in a single reactor.

Time (h)	CO_2 detected (μmol)	CO detected (μmol)	H_2 detected (μmol)	[a]Theoretical H_2 from CO_2 (μmol)	[b]Theoretical H_2 from CO (μmol)	[c]Theoretical H_2 in total (μmol)
2	0.12	0.03	0.34	0.28	0.05	0.33
4	0.30	0.06	0.72	0.69	0.07	0.77
6	0.38	0.07	1.08	0.90	0.09	0.99
8	0.52	0.09	1.40	1.22	0.12	1.34

[a] "Theoretical H_2 from CO_2" was calculated based on "CO_2 detected" and Eq. (12).
[b] "Theoretical H_2 from CO" was calculated based on "CO detected" and Eq. (13).
[c] "Theoretical H_2 in total" was the sum of "Theoretical H_2 from CO_2" and "Theoretical H_2 from CO".

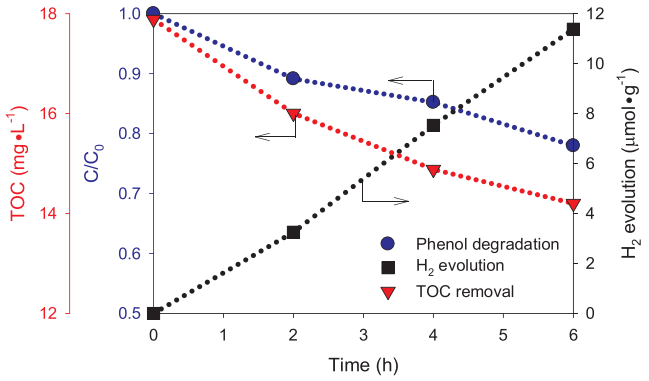

Fig. 10. Hydrogen production, phenol degradation and TOC change in the dual function reaction conducted in a twin-reactor. (Experimental conditions: hydrogen evolution side – 0.25 g Pt/STO:Rh was dispersed in 220 mL water containing 2 mM $FeCl_2$ (pH = 2.4); phenol oxidation side – 0.1 g WO_3 was suspended in 220 mL water containing 2 mM $FeCl_3$ (pH = 2.4); initial concentrations of phenol: 200 μmol L^{-1}; 300 W Xe Lamp equipped with an AM1.5 G filter; twin-reactor).

Table 3
The compositions of the gas phase in a single reactor and the two separate parts of the twin-reactor when conducting dual function reaction (phenol C_0 = 200 μmol L^{-1}).

Reactor type	Location	H_2 %	CO_2 %	CO %
Twin-reactor	Phenol removal side	6.0	83.0	11.0
	H_2 production side	94.0	5.0	1.0
Single reactor		70.0	25.0	5.0

were shown in Table 3. From the results, it was apparent that H_2 accounted for 70% while CO_2 and CO accounted for the rest of 30% of the gas phase when using a single reactor to conduct the dual function reaction. On the other hand, when using the twin-reactor to conduct the same reaction, H_2 accounted for 94% of the gas phase and only 6% was CO_2 and CO in the H_2 evolution side; for the phenol oxidation side, 94% was CO_2, CO while the rest of 6% was H_2. Compared to a single reactor, the utilization of a twin-reactor would separate the evolved H_2 from CO_2 and CO directly when it is produced, reducing the cost of further purification.

The effect of initial phenol concentration on the hydrogen evolution was investigated. The initial phenol concentrations were set to be 50, 100, 150 and 200 μmol L^{-1} in different experiments while other conditions remained the same. The H_2 yields in the 6-h reaction were shown in Fig. 11. When using pure water for water splitting, the H_2 yield was 9.49 μmol g^{-1}. For the dual function reactions with phenol addition, the H_2 yield was 10.57–11.37 μmol g^{-1}, all higher than that of the pure water splitting. The H_2 yield increased with the increase of phenol concentration and reached its maximum at C_0 = 200 μmol L^{-1}. The maximum hydrogen yield was 11.37 μmol g^{-1}, which was 20% larger than that of pure water splitting.

In order to evaluate a photo-excited reaction, especially in the solar energy utilization, photo quantum efficiency (PQE) has been determined as follows:

$$\mathrm{PQE}\,(\%) = \frac{\text{number of reacted electrons}}{\text{number of incident photons}} \times 100\,\% = \frac{2 \times \text{number of evolved } H_2 \text{ molecules}}{\text{number of incident photons}} \times 100\% \quad (14)$$

The incident photon amount was determined from the incident light intensity (28 mW•cm^{-2}, measured by the Goldilux radiometer/photometer (UV-A Probe/UV-C Probe) and the area of projected light irradiation (20 cm^2 for both the single and twin reactor). PQE of the single reactor and twin-reactor is 0.005% and 0.014%, respectively. The

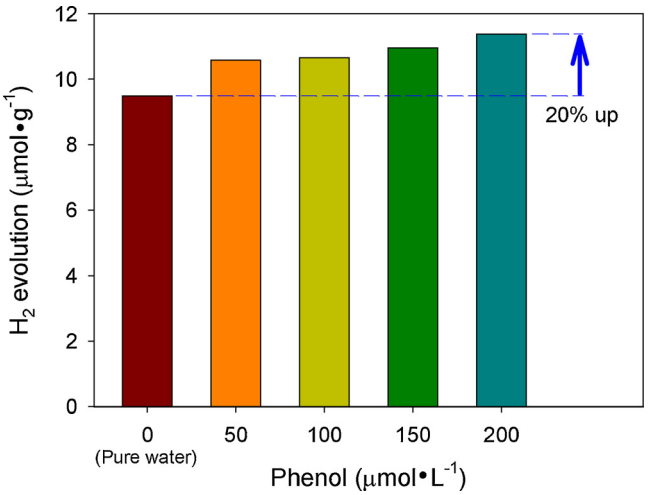

Fig. 11. Hydrogen generation amount in pure water splitting and dual function reaction with different phenol initial concentrations of phenol conducted in a twin-reactor. (Experimental conditions: hydrogen evolution side – 0.25 g Pt/STO:Rh was dispersed in 220 mL water containing 2 mM $FeCl_2$ (pH = 2.4); phenol oxidation side – 0.1 g WO3 was suspended in 220 mL water containing 2 mM $FeCl_3$ (pH = 2.4); initial concentrations of phenol: 0, 50, 100, 150, 200 μmol L^{-1}; 300 W Xe Lamp equipped with an AM1.5 G filter; twin-reactor).

photon energy was near 3 times effectively utilized to produce H_2 in the twin-reactor compared to in the single reactor.

The enhancement of hydrogen evolution could be explained from the kinetics perspective as shown in Fig. 12. Phenol acted as the hole scavenger of WO_3 in the dual function reaction, which would scavenge the holes on WO_3 and other oxidative species (e.g. H_2O_2, O_2 and OH•) in the system. Therefore, the electron-hole recombination on WO_3 would be avoided, and the efficiency of Fe^{3+} reduction to Fe^{2+} would be increased. At the same time, since the oxidative species in the system were scavenged by phenol, the re-oxidation of Fe^{2+} to Fe^{3+} was significantly avoided. All these effects would result in the increase of Fe^{2+} concentration and the decrease of Fe^{3+} concentration in the phenol oxidation side. Moreover, the diffusion rate of Fe^{2+} from the phenol oxidation side to the hydrogen evolution side through the Nafion membrane would be enhanced due to the large concentration gradient, which was same for Fe^{3+} to diffuse from the hydrogen evolution side to the phenol oxidation side. In the hydrogen evolution side, the Fe^{2+} concentration would increase and Fe^{3+} decrease. For the hydrogen evolution half reaction, Fe^{2+} was the hole scavenger of Pt/STO:Rh which would avoid the recombination of electron-hole pairs on Pt/STO:Rh and enhance the reduction efficiency of photo-induced electrons. Overall, the counter diffusion of Fe^{2+}/Fe^{3+} would reach dynamically steady state, which also matches the kinetic rate of H_2 evolution. As a result, for the dual function reaction with phenol addition, the H_2 yield in the 6-h reaction was all higher than that of the pure water splitting under the same conditions. Moreover, the H_2 yield would increase with increasing phenol concentration. These results are in agreement with previous studies of organic dyes [36], biomass [37], glycerol [38], and organic acids [39,40].

4. Conclusions

In this study, solid-state fusion method and photo-deposition method were successfully utilized to prepare the hydrogen evolution photocatalyst Pt/STO:Rh. The results showed that the Pt/STO:Rh had perovskite structure and excellent crystallinity. The energy bandgap was noticeably decreased to 2.4 eV by the doping of Rh so that the prepared Pt/STO:Rh photocatalyst could be excited by artificial sunlight. The dual function reaction of H_2 evolution and simultaneous phenol degradation was conducted in a single reactor, and a twin

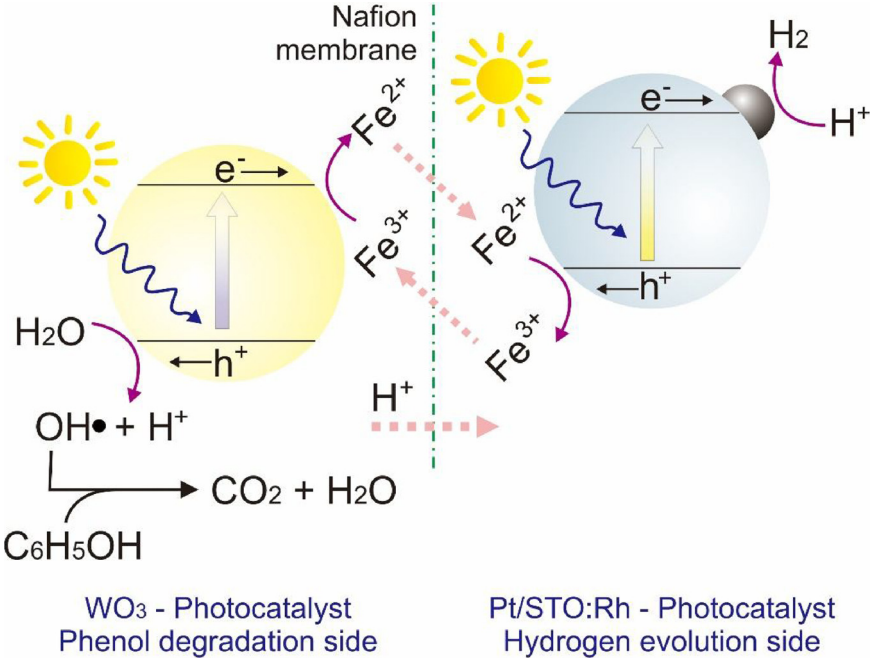

Fig. 12. The diagram of a modified Z-scheme mechanism for dual function reaction for photocatalytic degradation of phenol and simultaneous hydrogen production.

reactor, respectively, with WO_3 and Pt/STO:Rh as photocatalysts under a simulated sunlight AM1.5 G, and Fe^{3+}/Fe^{2+} pairs were utilized as the electron mediators. Two kinds of photocatalysts were divided by the Nafion membrane in the twin reactor. The photocatalytic efficiency was substantially increased due to the inhibition of backward reaction by separating H_2 from the products directly. The H_2 production rate was raised to 1.90 μmol g^{-1} h^{-1} and the phenol (C_0 = 200 μmol L^{-1}) degradation was increased to 22% within 6 h. Furthermore, the concentration of H_2 increased from 70% in the single reactor to 94% in the twin-reactor (hydrogen evolution side). Such direct separation of H_2 from other gaseous products would significantly save the cost of purification. Finally, the energy release from phenol oxidation can supply the energy requirement of water splitting for H_2 production. Our result showed that coupled with phenol oxidation; the hydrogen yield was 20% higher than that of the pure water splitting. Additionally, the photon energy was more effectively utilized to produce H_2 in the twin-reactor compared to in the single reactor. The PQE of the single reactor and twin-reactor is 0.005% and 0.014%, respectively.

Although many efforts have been made so far to promote photocatalysis, this approach still faces several challenging issues: (1) currently reported photocatalysts suffer from low photo quantum efficiency (PQE); and (2) the some detailed photocatalytic kinetic mechanism remains unclear in our twin-reactor. Therefore, in the future research, efforts shall pay attention on: (1) developing more efficient photocatalysts (a wide optical absorption band, a low recombination rate of e^-/h^+ pairs); (2) revealing the relationship between the structural architecture and the photocatalytic activity to elucidate the photo-mechanisms and surface photo-reaction pathways.

Acknowledgments

The authors gratefully acknowledge financial support from the Taiwan Ministry of Science and Technology under project MOST 105-2221-E-002-206-MY3 and the National Natural Science Foundation of China, Grants No. U1305242.

Appendix A. Supplementary data

Supplementary material related to this article can be found, in the online version, at doi:https://doi.org/10.1016/j.apcatb.2018.08.010.

References

[1] A. Kudo, Y. Miseki, Chem. Soc. Rev. 38 (2009) 253–278.
[2] K. Maeda, K. Teramura, D.L. Lu, T. Takata, N. Saito, Y. Inoue, K. Domen, Nature 440 (2006) 295–295.
[3] K. Maeda, K. Domen, J. Phys. Chem. Lett. 1 (2010) 2655–2661.
[4] A. Fujishima, K. Honda, Nature 238 (1972) 37 − +.
[5] C.C. Lo, C.W. Huang, C.H. Liao, J.C.S. Wu, Int. J. Hydrogen Energy 35 (2010) 1523–1529.
[6] H. Park, C.D. Vecitis, W. Choi, O. Weres, M.R. Hoffmann, J. Phys. Chem. C 112 (2008) 885–889.
[7] K. Sayama, K. Mukasa, R. Abe, Y. Abe, H. Arakawa, J. Photochem. Photobiol. A-Chem. 148 (2002) 71–77.
[8] S. Sun, W. Wang, D. Li, L. Zhang, D. Jiang, ACS Catal. 4 (2014) 3498–3503.
[9] O. Neufeld, N. Yatom, M. Caspary Toroker, ACS Catal. 5 (2015) 7237–7243.
[10] Q. Zhang, Z. Li, S. Wang, R. Li, X. Zhang, Z. Liang, H. Han, S. Liao, C. Li, ACS Catal. 6 (2016) 2182–2191.
[11] S. Ahmed, M.G. Rasul, W.N. Martens, R. Brown, M.A. Hashib, Desalination 261 (2010) 3–18.
[12] M.N. Chong, B. Jin, C.W.K. Chow, C. Saint, Water Res. 44 (2010) 2997–3027.
[13] U.I. Gaya, A.H. Abdullah, J. Photochem. Photobiol. C-Photochem. Rev. 9 (2008) 1–12.
[14] K. Maeda, ACS Catal. 3 (2013) 1486–1503.
[15] S.C. Yu, C.W. Huang, C.H. Liao, J.C.S. Wu, S.T. Chang, K.H. Chen, J. Membr. Sci. 382 (2011) 291–299.
[16] Z. Pan, T. Hisatomi, Q. Wang, S. Chen, M. Nakabayashi, N. Shibata, C. Pan, T. Takata, M. Katayama, T. Minegishi, A. Kudo, K. Domen, ACS Catal. 6 (2016) 7188–7196.
[17] H. Suzuki, S. Nitta, O. Tomita, M. Higashi, R. Abe, ACS Catal. 7 (2017) 4336–4343.
[18] W.H. Lee, C.H. Liao, M.F. Tsai, C.W. Huang, J.C.S. Wu, Appl. Catal. B 132 (2013) 445–451.
[19] J. Kim, W. Choi, Energy Environ. Sci. 3 (2010) 1042–1045.
[20] J. Kim, D. Monllor-Satoca, W. Choi, Energy Environ. Sci. 5 (2012) 7647–7656.
[21] Y.J. Cho, H.I. Kim, S. Lee, W. Choi, J. Catal. 330 (2015) 387–395.
[22] J. Kim, Y. Park, H. Park, Int. J. Photoenergy (2014) 9.
[23] J.P. Zou, D.D. Wu, S.K. Bao, J.M. Luo, X.B. Luo, S.L. Lei, H.L. Liu, H.M. Du, S.L. Luo, C.T. Au, S.L. Suib, ACS Appl. Mater. Interfaces 7 (2015) 28429–28437.
[24] R. Konta, T. Ishii, H. Kato, A. Kudo, J. Phys. Chem. B 108 (2004) 8992–8995.
[25] K. Wenderich, G. Mul, Chem. Rev. 116 (2016) 14587–14619.
[26] V.-H. Nguyen, S.D. Lin, J.C.-S. Wu, H. Bai, Beilstein J. Nanotechnol. 5 (2014) 566–576.
[27] D. Chen, J. Ye, Chem. Mater. 19 (2007) 4585–4591.
[28] M. Yoshino, M. Kakihana, W.S. Cho, H. Kato, A. Kudo, Chem. Mater. 14 (2002) 3369–3376.
[29] K. Maeda, K. Teramura, D. Lu, N. Saito, Y. Inoue, K. Domen, Angew. Chem. 118 (2006) 7970–7973.
[30] H. Tada, T. Kiyonaga, S. Naya, Chem. Soc. Rev. 38 (2009) 1849–1858.
[31] C.D. Jaeger, A.J. Bard, J. Phys. Chem. 83 (1979) 3146–3152.

[32] M. Stylidi, Appl. Catal. B 47 (2004) 189–201.
[33] M. Barakat, H. Schaeffer, G. Hayes, S. Ismat-Shah, Appl. Catal. B 57 (2005) 23–30.
[34] K. Parida, S. Dash, D. Das, J. Colloid Interface Sci. 298 (2006) 787–793.
[35] S. Esplugas, J. Gimenez, S. Contreras, E. Pascual, M. Rodríguez, Water Res. 36 (2002) 1034–1042.
[36] A. Patsoura, D.I. Kondarides, X.E. Verykios, Appl. Catal. B 64 (2006) 171–179.
[37] D.I. Kondarides, V.M. Daskalaki, A. Patsoura, X.E. Verykios, Catal. Lett. 122 (2007) 26–32.
[38] V.M. Daskalaki, D.I. Kondarides, Catal. Today 144 (2009) 75–80.
[39] V.M. Daskalaki, M. Antoniadou, G.L. Puma, D.I. Kondarides, P. Lianos, Environ. Sci. Technol. 44 (2010) 7200–7205.
[40] A. Patsoura, D.I. Kondarides, X.E. Verykios, Catal. Today 124 (2007) 94–102.